



Mechanical performance of nanosilica filled quartz fiber/polyimide composites at room and elevated temperatures

Jie Wang^{1,*}, Wancheng Zhou¹, Fa Luo¹, Dongmei Zhu¹, and Yuchang Qing¹

¹ State Key Laboratory of Solidification Processing, Northwestern Polytechnical University, Xi'an 710072, Shaanxi, China

Received: 13 March 2017

Accepted: 29 June 2017

Published online:
10 July 2017

© Springer Science+Business
Media, LLC 2017

ABSTRACT

The polyimide (PI) composites reinforced with silanized nanosilica (SNS) and/or quartz fabrics had been fabricated. Influences of the SNS dispersion on morphology, Vickers hardness, thermal stability and mechanical properties of these composites were studied. The uniform dispersion of SNS in PI resulted from the crosslink of silane pretreated on the surface of nanosilica and PI chains. The measurement results indicated that density, Vickers hardness and flexural strength were enhanced due to the addition of SNS into the PI matrix and the optimum content of SNS was 2 wt%. The thermal stability of the SNS reinforced PI composites increased with an increase in weight fraction of SNS, compared with the neat PI resin. The effects of quartz fabric on the mechanical properties of quartz fabric-reinforced PI composites with different volume fractions and effects of post-curing on the flexural strength were also investigated. Results also showed that better mechanical properties of quartz fabric-reinforced PI composites were obtained when the volume fraction of quartz fabric was 50%. The quartz fabric-reinforced PI composites containing 2 wt% SNS after post-curing exhibited the highest flexural strength and elasticity modulus by virtue of good fiber-matrix interface, and flexural strength was almost 500 MPa at 300 °C. It is pointed that the composites have a great application prospect as one of engineering materials with high strength and high temperature resistance.

Introduction

In recent years, the study on conventional fiber reinforced polymer-matrix (FRP) composites with various types of nanofillers has drawn significant attention from both academia and industry [1–4]. Laminated composites exhibit poor matrix

dominated and mechanical properties often susceptible to various harsh and hostile environments [5–7]. Few studies have suggested that the mechanical response of these potential materials is significantly altered when they are exposed to elevated temperature environment [8, 9]. Incorporation of nanofiller such as aluminum oxide (Al₂O₃), titanium dioxide

Address correspondence to E-mail: wangjienwpu896@163.com

(TiO₂), silicon dioxide (SiO₂), zirconium dioxide (ZrO₂) nanoparticles [10–14] has been successfully used to improve the matrix dominated and mechanical properties. Nanosilica fillers with the attractive characteristics of extremely large surface area can not only improve the mechanical and tribological properties but also have additional functional properties such as atomic oxygen (AO) resistance, electrical and thermal conductivity [13–15], which can enrich the functions of the nanocomposites to achieve the desirable characteristic for low earth orbit space applications [16]. However, adding nanosilica to the FRP composites has its own challenges. The main challenge is to disperse them uniformly in the polymer matrix in order to obtain high interfacial area where stress can be transferred from the weak matrix to the strong nanoparticles [17, 18]. Effective stress which transfers through the nanosilica/polymer interface is the key factor to obtain superior mechanical properties in the nanosilica modified laminated composites [19]. Various methods have been demonstrated in the literature to disperse the nanosilica in polymer resin such as silanization, stirring and sonication [13–18]. The silanization is an often used method that serves a bridging unit for the nanoparticles. It forms interphase links through the hydrolysis and condensation reactions of alkoxy silane groups, and the simultaneous polymerization of resin groups [16].

Owing to outstanding combination performance of thermal, mechanical, chemical resistance and dielectric properties [20, 21], PI materials not only is applied in electric industries, especially in high electric field and high temperature application, but also is applied to aerospace industries [22–24]. Thus, PI material is a promising matrix candidate for FRP composites due to the dramatic mechanical property improvements by introducing only a small fraction of inorganic additives [25, 26]. However, the recent researches were mainly focused on the preparations of polyimide-silica hybrid films [27, 28] and silica/polyimide nanofiber membranes [29, 30], also tribological, optical, tensile properties and fracture toughness of fiber reinforced polyimide with nanosilica composites [25, 26]. John Montesano et al. [8] investigated the failure mechanism in a triaxially braided polyimide composite at room and elevated temperature. In addition, few reports attempt to characterize the flexural strength of fiber/polyimide

with nanosilica composites at elevated temperature. The objective of this study is to investigate the mechanical behavior and fracture mechanism for quartz fiber reinforced polyimide with nanosilica composites. Particular emphasis is placed on determining the influences of the volume fraction of fiber and content of nanosilica on mechanical properties. Data of physical, thermal properties and Vicker hardness is also included to provide an understanding of how the matrix performances are affected by addition of nanosilica.

Experimental

Materials

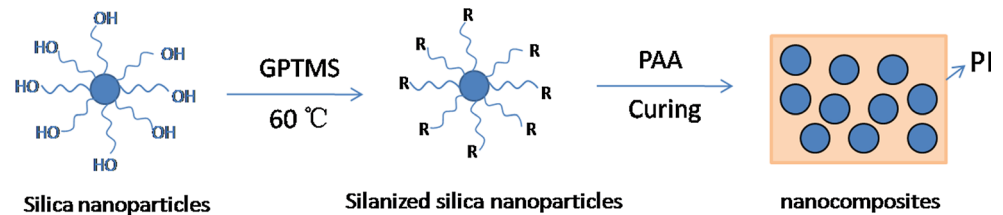
Poly (amic acid) solution (PAA) (solids concentration 40%) was supplied by Changchun Institute of Applied Chemistry, Jilin, China. This high temperature PI resin was prepared by the modified polymerization monomeric reactants method (MPMR) endcapped with phenylethynyl. The quartz fabrics were provided by Hubei Feilihua Quartz Glass Co. Ltd. China. The specific details of quartz fabrics are described in our previous literature [31]. The SiO₂ NPs were provided by Hangzhou Wan Jing New Material Co., Ltd. China. General characteristics of SiO₂ NPs were described in Table 1. Anhydrous ethanol and 3-glycidoxypropyl trimethoxysilane (GPTMS, 98%) were received from Sinopharm Chemical Reagent Co., Ltd, Shanghai, China. *N,N'*-dimethylacetamide (DMAc) was provided by Tianjin Fu Chen Chemical Reagents Factory.

Silanized treatment of SiO₂ NPs

First, ultrasonic waves and a high-speed homogenizer were used to disperse 10 g of silica nanoparticles homogeneously in 50 ml of ethanol solution. And then 12.0 ml of GPTMS and 3.8 ml of deionized water were added to the mixture under magnetic stirring for 2 h and hydrochloric acid was added dropwise until the value of PH was equal to 2. Next, the mixture was stirred reversely for 48 h. Silanized nanosilica (SNS) were then collected by centrifugation with ethanol for three times and deionized water for twice and vacuum-dried at 60 °C for 16 h. The preparation was illustrated in Fig. 1.

Table 1 Properties of the SiO₂ NPs

Name	Type	SiO ₂ Content (%)	Diameter (nm)	Surface area (m ² /g)	The value of PH	Conduction (W/mK)
SiO ₂ NPs	VK-SP50	99.5	50 ± 5	200 ± 30	5–7	1.46

Figure 1 Representative schemes of the preparation of silanized silica nanoparticles and nanocomposites. R is the organic functional group.

Sample preparation

Quartz fabrics reinforced PI composites

The fabrication of quartz fabric reinforced PI composite (QFRP) specimens was done in two stages. In the first stage, the fabrics were dipped into PAA solution for 30 min in vacuum in order to achieve better penetration of matrix into the openings of the fabrics. After infiltration, the fabrics were dried in a vacuum oven at 150 °C for 4 h, which was conducive to the solvent evaporation and thermal imidization of PAA. In the second stage, the mixtures were placed into a square metal die and a pressure of 8 MPa was applied when the temperature reached 270 °C with a heating rate of 4 °C/min. After that, the temperature increased to 370 °C for 1 h with applied pressure for the formation of the composites. QFRP composites untreated and treated with post-curing were termed as UQFRP and TQFRP. QFRP composites were fabricated with different volume fraction of quartz fabrics of 45% (16 layers of fabrics), 50% (18 layers of fabrics) and 55% (20 layers of fabrics), which were termed as 16UQFRP, 18UQFRP and 20UQFRP. Finally, only 18 layers of fabrics reinforced PI composites (18TQFRP) were removed in the oven at 370 °C for 3 h for post-curing, because it exhibited the best performance among all quartz fabric layers.

Nanocomposites

The weight fraction ranging from 1, 2 and 3 wt% of the silanized SiO₂ NPs were dispersed in DMAc solvent using an ultrasonic bath at room temperature for 2 h. Then the DMAc-based solution was dispersed with the PAA solution, followed by the sonication and accompanied by mechanical stirring for 5 h. In order to evaporate the solvent and fulfill the

imidization, the mixtures were placed in vacuum oven at 120 °C for 1 h and 240 °C for 2 h. Next, the mixtures were grounded into fine powder after heat treatment. At last, the powders were cured with a pressure of 5 MPa for the formation of insoluble and cross-linked polyimide/hybrid fillers composites with a thickness of 3 mm. The nanocomposites containing 1, 2 and 3 wt% silanized SiO₂ NPs were termed as PSNS1, PSNS2 and PSNS3, respectively. The PI without SiO₂ NPs was considered as a control.

Quartz fabric reinforced nanocomposites

Eighteen layers of woven quartz fabric were used for composite laminate preparation, with the volume fraction of 50% quartz fiber and 50% resin matrix. The fabrication steps are similar to that of TQFRP described before. The quartz fabric reinforced nanocomposites containing 1, 2 and 3 wt% silanized SiO₂ NPs were termed as TQFR-PSNS1, TQFR-PSNS2 and TQFR-PSNS3, respectively. The mix proportions are shown in Table 2.

Characterization

Scanning electron microscopy (SEM)

Scanning electron microscopy imaging was obtained using a JEOL JSM-5800 LV SKANNING. The SEM investigation was carried out in detail on microstructures and fracture surfaces of samples after three-point bending and impact strength tests.

Thermogravimetric analysis (TGA)

The thermal stability of samples was studied by thermogravimetry analysis (TGA). A Q-600 analyser (TA instruments-Waters LLC) was used for all

Table 2 Mix proportions of specimens

Sample	Quartz fabric (QF)		Mix proportions (wt%)		Whether treated with post-curing
	Volume fraction (%)	Fabric layers	Polyimide	SNS	
PI	0	0	100	0	Untreated
16UQFRP	45	16	100	0	Untreated
18UQFRP	50	18	100	0	Untreated
20UQFRP	55	20	100	0	Untreated
18TQFRP	50	18	100	0	Treated
PSNS1	0	0	99	1	Untreated
PSNS2	0	0	98	2	Untreated
PSNS3	0	0	97	3	Untreated
18TQFR-PSNS1	50	18	99	1	Treated
18TQFR-PSNS2	50	18	98	2	Treated
18TQFR-PSNS3	50	18	97	3	Treated

measurements. Samples with 10 mg were placed in an alumina crucible and were heated from 20 to 1000 °C with a heating rate of 10 °C/min. All experiments were carried out in nitrogen atmosphere.

Physical properties

The Vickers hardness measurements were performed using a FV-1000 device (Shanghai Caikon optical instrument Co., Ltd). The hardness values were measured immediately after the indentation with a 0.1 kg load for 10 s. Archimedes principle was employed to measure the open porosity and bulk density, which were conducted to determine the quality of nanocomposites.

Mechanical properties

Three-point bending test (specimen size of 60 l mm × 10w mm × 3t mm) was carried out at ambient temperature with a cross-head speed of 1.5 mm/min and support span length of 48 mm using a universal testing machine (Haida Qualitative Analysis, HD-609B). Each sample was short not suitably in 5. The flexural strength (σ) was calculated by the following equations:

$$\sigma = \frac{3FL}{2bh^2} \quad (1)$$

where F is the load on the force–displacement curve, L is the support span length, b is the specimen width, and h is the specimen thickness.

Results and discussion

Effect of SNS weight fraction on physical properties of nanocomposites

Morphologies

Generally, morphology and distribution of the loading particles in polymeric matrices have an important effect on the overall performance of nanocomposites [32]. Therefore, the SEM was used to examine the morphologies of the prepared composites. Figure 2a–d show the fractured surfaces images of representative composites. Figure 1a depicts morphology of the neat PI, which shows that the PI is uniform. The SEM images of the fractured surface of PSNS1 and PSNS2 in Fig. 2b and c show almost perfect nanoparticle dispersion. Meanwhile, the SNS on the surface (partially marked by arrows in Fig. 2b and c can be detected and the dispersed SNS have a greater mean size i.e. 80 nm if the particle size is compared with nanoparticles (average 50 nm), due to the core–shell of particles were coated with layer of polymer chains [33]. It is interesting to note that numerous nanoparticles are embedded in the PI matrix and a good interface adhesion between PI matrix and nano-sized particles is obtained. Moreover, the distance between particles seems to become short and space between particles becomes narrow with the increase in SNS content, which implies that the interaction between PI chains and particles became strong [28]. As the SNS was added with 3 wt%, a proper dispersion cannot be observed due to the aggregations

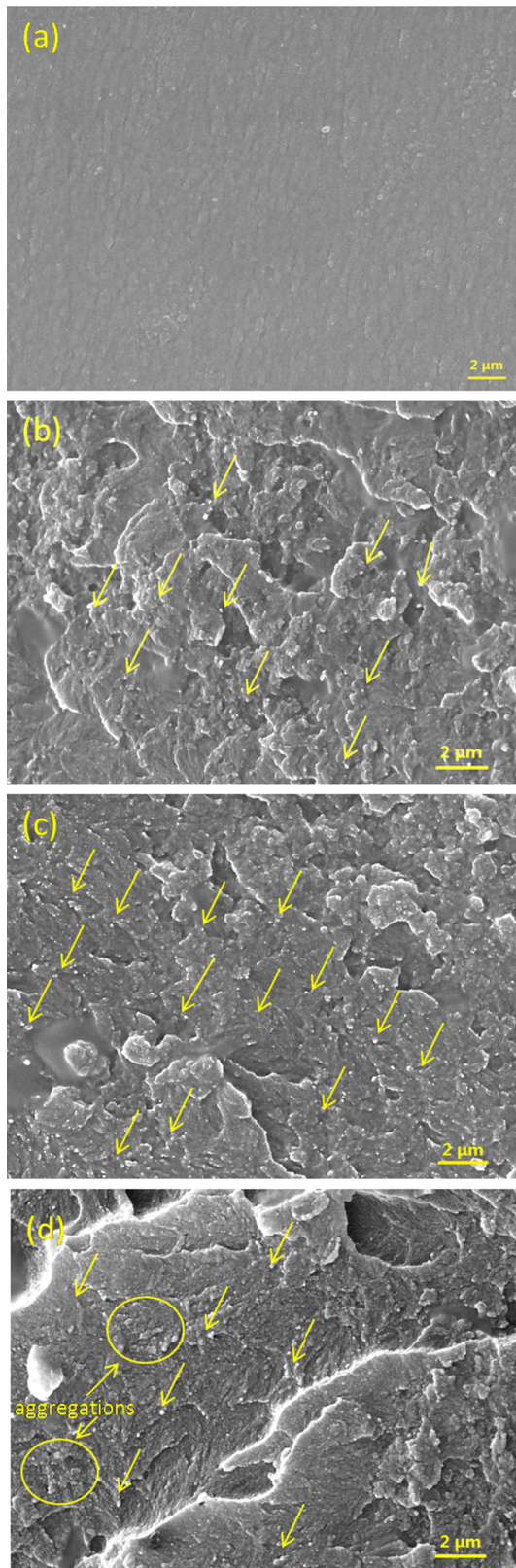


Figure 2 SEM micrographs of **a** PI, **b** PSNS1, **c** PSNS2 and **d** PSNS3 from the cross-section of fracture surface.

of SNS and a lot of larger particles (up to 120 nm) in composites clearly appeared in Fig. 2d, which has a negative effect on the sample properties. This may be attributed to the strong interaction of silica–silica spheres. It infers that sonication and mechanical stirring mixing method does not provide enough energy so that it can break up all strong inter-connected SiO₂–SiO₂ NPs. Basically, the SEM images suggest that the SNS with a proper content are dispersed uniformly in the PI matrix.

Porosity, density and Vickers hardness of nanocomposites

The porosity and density of nanocomposites are shown in Table 3. As expected for all PSNS nanocomposites, the porosity decreases and the density increases with increasing SNS content as compared to PI bulk. It indicates that the SNS has filling effect in the porosity resulting from the escaped gas during the period of matrix curing. Typical Vickers indents in PI and PSNS2 composites under a 0.1 kg load are presented in Fig. 3. It is clear that the indents in the pure PI resin are consistently larger than those in the PSNS2 under the same loading conditions. In addition, a star-shaped Vickers impression is observed in the PSNS2, whereas the PI exhibits a pyramidal impression. The measured values of the Vickers hardness (H_v) of PI and PSNS are listed in Table 3. Here, ten measurements were performed on different spots all over each sample and used for the determination of average values of H_v . The evaluated hardness of PI is 0.37 GPa. With SNS loading, the hardness increased significantly at different concentrations, the highest value for hardness being attained by the PSNS2. Further, we observe a decrease in the Vickers hardness of PSNS3. The poor dispersion of SNS in the matrix is the main reason for this decrease in hardness and with a higher SNS loading (3 wt%) evidenced by morphology studies [34].

Table 3 Measured Vickers hardness of nanocomposites

Samples	Density (10^3 kg/m^3)	Porosity (%)	H_v (GPa)
PI	1.34 ± 0.02	1.92 ± 0.04	0.37
PSNS1	1.35 ± 0.01	1.81 ± 0.02	0.41
PSNS2	1.36 ± 0.02	1.61 ± 0.03	0.46
PSNS3	1.36 ± 0.01	1.75 ± 0.06	0.44

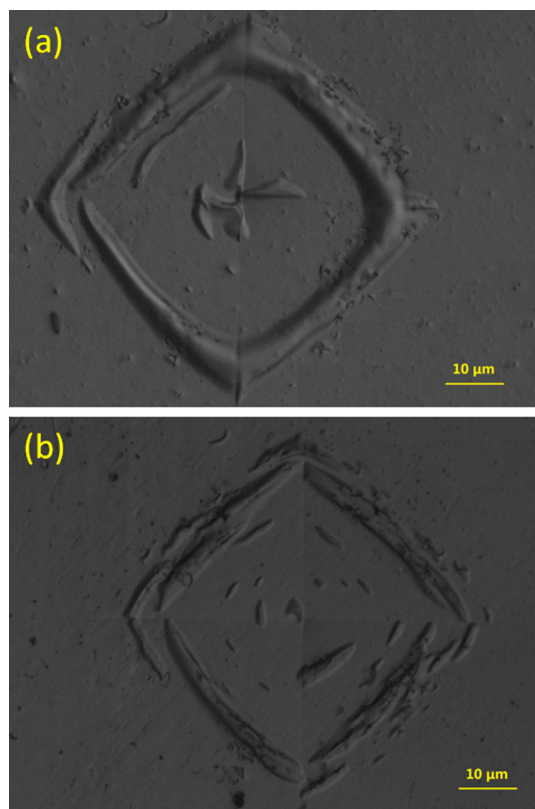


Figure 3 Scanning electron micrographs revealing the typical morphology of 0.1 kg Vickers indent for **a** PI and **b** PSNS2.

Thermal analysis

Thermal stability is an essential property for engineering materials, and the limiting factor of both processing and applications. The thermal properties of PI and PSNS nanocomposites were analyzed by TGA analysis as listed in Table 4. Meanwhile, the thermal stability behavior was illustrated in Fig. 4.

Table 4 Thermal properties of nanocomposites and neat PI^a

Samples	T_{d5}^a (°C)	T_{d20}^a (°C)	CR ^b (%)	TMR ^c (°C)
SNS	/	/	97.9	/
PI	533.0	597.1	69.2	582.7
PSNS1	531.9	601.4	69.6	584.5
PSNS2	539.6	606.5	70.3	585.9
PSNS3	537.8	606.0	71.3	585.1

^a Temperature at which 5 and 20% weight loss recorded by TGA at a heating rate of 10 °C/min in a nitrogen atmosphere

^b Percentage weight of material left undecomposed after TGA analysis at temperature 800 °C in a nitrogen atmosphere

^c Temperature at maximum rate of weight loss recorded by TGA at a heating rate of 10 °C/min in a nitrogen atmosphere

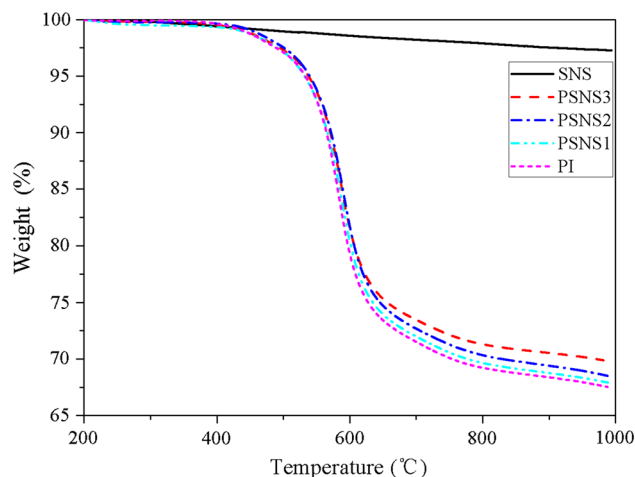


Figure 4 TGA curve of the SNS powders, PI and PSNS composites.

The SNS decomposes slowly from 200 °C and show less than 3 percent loss in weight before 800 °C under nitrogen, probably due to the loss of silane on the surface of the SNS. All samples with different contents of SNS exhibit excellent thermal stability and pristine PI prevent itself from thermal decomposition until 533 °C. The 5 wt% of decomposition temperature (T_{d5}) of the PSNS nanocomposites, increases with increasing SNS content, and shift from 533.0 °C (PI) to 539.6 °C (PSNS2), as shown in Table 3. This may be related to the higher thermal conductivity of SiO₂ that facilitate heat dissipation within the composites, hence preventing the accumulation of heat at certain points for degradation [35]. However, the T_{d5} increases with the increase of SNS content up to 2 wt% and is followed by a slight decrease for 3 wt% of SNS. A slight decrease in T_{d5} of PSNS3 compared to PSNS2 may be due to the non-homogeneous dispersion of SNS in PI matrix for high content of particles. Mostly, the incorporation of foreign particles in PI reduces its cross-linking density to some extent especially when the particle content is high and the reduction in cross-linking density results in lower decomposition temperature [36]. The 20 wt% of decomposition temperatures (T_{d20}) were also listed in Table 4. The highest thermal decomposition temperature of 606.5 °C can be achieved with 2 wt% of SNS. It indicates that SNS reduces the degradation of PI at high temperature as clearly seen in the curves. Since SNS are not decomposed at 800 °C, the char residue (CR) are retarded with increasing SNS content while the stoichiometry of the PI matrix is maintained [36]. Therefore, it could be verified that a small amount of

SNS acted as effective thermal degradation resistant reinforcement in the PI matrix, increasing the thermal stability of PSNS nanocomposites.

Three-point bending test at room temperature

The three-point bending test is used to determine the flexural strength and modulus of elasticity for the PI, UQFRP composites, 18TQFRP composites, PSNS nanocomposites and 18TQFR-PSNS composites. The results are shown in Table 5. It can be seen that flexural strength increases with the increase of SNS content up to the optimum SNS content, and then decreases after this limit. The optimum SNS content is 2 wt%, in which the averaged flexural strength and modulus of elasticity increases from 25.6 to 78.6 MPa and from 5.7 to 8.2 GPa, about 207 and 44% increase respectively compared to the neat PI. Figure 5 shows typical strength-deflection curves of the samples under investigation. All the specimens show a linear response until the brittle fracture occurring as illustrated in Fig. 5. This Figure shows clearly that besides the increase of stiffness and strength the elastic behavior (flexure extension) of nanocomposites is not suffering the existence of hard and brittle particles and can even increase significantly. The SNS loading in the PI matrix form the interfaces with the polymer chain and the polymer chain mobility at the nanoparticles surface interaction enhance the toughness of the PI matrix [13]. This effect separates nanocomposites from composites based on micro-scale particle fillers [37]. However, beyond this optimum content of SNS, the flexural strength of the composites decreases as the material becomes brittle and loses its ability to absorb the crack energy. At low

magnifications, the fracture surfaces of the samples in Fig. 6 show the presence of brittle fracture paths respectively specific step structure. As shown in Fig. 6a, the fracture surface of pure PI is flat and smooth, where a few cracks on. The number of cracks increases unexpectedly with 1 wt% SNS loading and the fracture surface is also observed to be flat in Fig. 6b. However, in PSNS2 (Fig. 6c), riverlines are observed on the fracture surface of PSNS2. Increasing number of river line markings roughly represents the number of isolated well dispersed SNS [1]. Furthermore, it can be seen that there is a SNS particle at the crack deflection. Crack deflection process at SNS particles in a matrix is proposed to play a significant role in resulting composite [38]. This theory assumes that a crack can be deflected at an obstacle and then can be forced to move out of initial crack propagation plane by tilting as well as twisting. This process leads

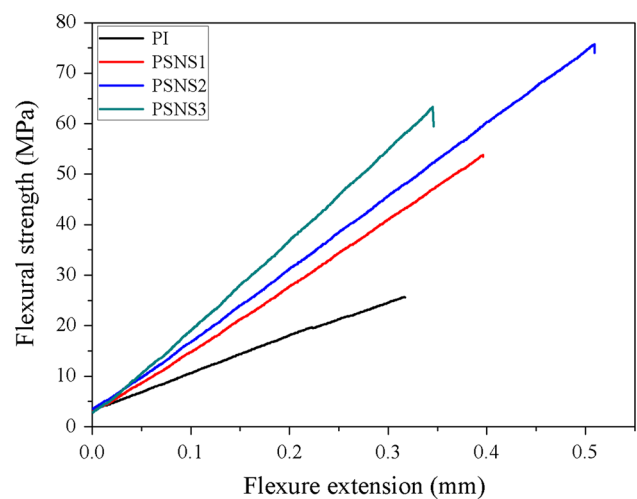


Figure 5 Strength-extension curves of PSNS nanocomposites and neat PI.

Table 5 The flexural strength and modulus of elasticity (E) of samples

Samples	Flexural strength (MPa)	Elasticity modulus (GPa)
PI	25.61 ± 6.02	5.71 ± 0.40
16UQFRP	761.11 ± 40.85	24.36 ± 0.89
18UQFRP	796.35 ± 38.21	25.19 ± 0.69
20UQFRP	729.78 ± 37.06	25.01 ± 0.68
18TQFRP	848.21 ± 30.05	25.78 ± 0.47
PSNS1	57.92 ± 4.87	7.72 ± 0.34
PSNS2	78.64 ± 8.06	8.25 ± 0.31
PSNS3	66.14 ± 8.53	9.17 ± 0.42
18TQFR-PSNS1	886.36 ± 41.23	25.98 ± 0.56
18TQFR-PSNS2	986.63 ± 59.60	26.85 ± 0.38
18TQFR-PSNS3	816.58 ± 48.86	25.20 ± 0.63

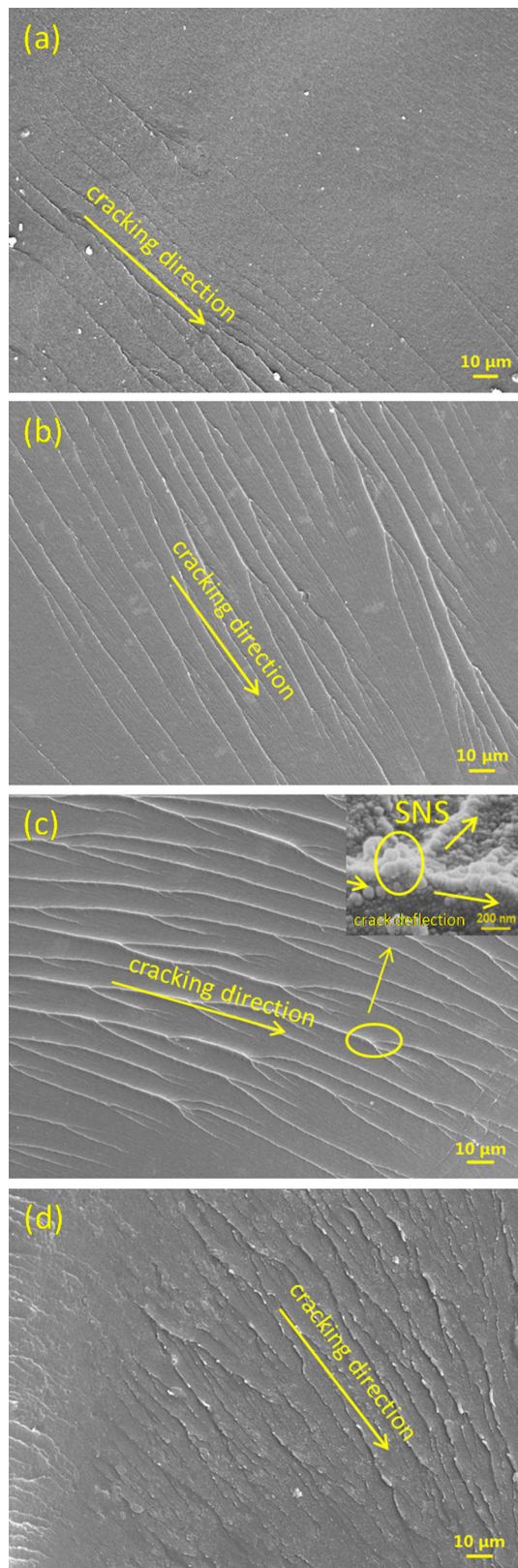


Figure 6 Fracture surface of **a** PI, **b** PSNS1, **c** PSNS2 and **d** PSNS3 by three-point bending test.

to an enhancement in total fracture surface area and thus absorbs extra energy compared to neat polymer matrices. In Fig. 6d, it can be observed that the material becomes brittle which causes multiple fractured rupture zones in it [34].

A similar trend is observed in the effect of quartz fabrics and SiO₂ NPs on the flexural strength of the composites. The optimum volume fraction of quartz fabric was found to be 50%, in which the flexural strength is up to 796.3 MPa. However, beyond this optimum volume fraction, the flexural strength of the composites decreases due to the poor adhesion between the fibers and the matrix [18]. In addition, Table 5 also shows the effect of the post-curing of composites on the flexural strength of 18TQFRP composites. It is clearly seen that the flexural strength and modulus of elasticity of 18TQFRP composites increase from 796.3 to 848.2 MPa and from 25.2 to 25.8 GPa, about 6.5 and 2.4% increase respectively compared to 18UQFRP composites. Since the magnitude of modulus is related to the molecular weight, it is believed that additional cross-linking occurs at the period of post-curing due to further inorganic condensation reactions and covalent bonding with the polyimide [39]. The fracture surface morphologies for the three-point bending test of 18UQFRP and 18TQFRP samples are shown in Fig. 8a and b. The SEM micrograph of 18UQFRP sample (Fig. 8a) shows that the fibers are torn out or debonded from the matrix because of poor interaction between the matrix and fibers and micro-gaps are present between the fibers during the three-point bending test [34]. After the post-curing, the interaction between the matrix and the fibers is improved but the fibers are still debonded from the matrix marked by yellow arrows in Fig. 8b.

Overall, the incorporation of SNS into the 18TQFRP composites lead to a significant enhancement in the flexural strength of all quartz fabrics reinforced nanocomposites. The flexural strength of 18TQFR-PSNS2 increases from 848.2 to 986.6 MPa, about 16.3% increase compared to 18TQFRP composites. Table 5 shows that the 18TQFR-PSNS3 obtained a lower flexural strength and modulus of elasticity than the other PSNS, evidencing the previous comment on the thermal analysis. The Strength-extension curves of 18TQFR-PSNS composites show a more ductile behavior as compared to 18TQFRP samples, as depicted in Fig. 7. The stiffness and flexural strength follows an ascending trend until the 18TQFR-PSNS2

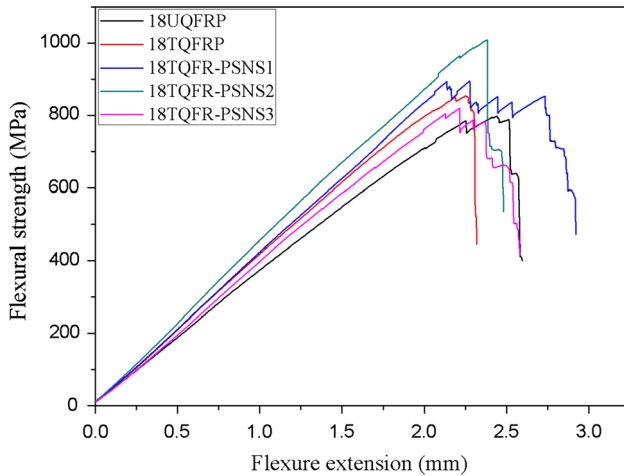


Figure 7 Strength-extension curves of 18UQFRP, 18TQFRP and 18TQFR-PSNS composites.

then it declines for the 18TQFR-PSNS3. Figure 8c and d show the SEM micrographs of the fiber-matrix interface of 18TQFR-PSNS2 and 18TQFR-PSNS3 composites after three-point bending test. The examination of fracture surface of 18TQFR-PSNS2 composites shows good fiber-matrix interfacial bonding (in Fig. 8c), which reveals that good fiber-nanomatrix interface is achieved. However, the SEM image of 18TQFR-PSNS3 composites (Fig. 8d) shows relatively poor adhesion between the fiber and the matrix as well as debonding. The interaction between PI and SNS as well as on the fiber-matrix interface is characterized in more details as shown in Fig. 9. The SEM images of 10 thousand times magnification in Fig. 9a and b show the good PI-SNS interfacial bonding on the fiber-matrix interface, indicating the energy can be transferred effectively between SNS and matrix [38]. Figure 9a shows the SNS of 18TQFR-PSNS2 are dispersed uniformly on the fiber-matrix interface, and it is clear that there are regions with poor dispersion and presence of aggregates in Fig. 9b. This result indicates that the nanomatrix of 18TQFR-PSNS3 becomes brittle and loses its ability to hold the fibers together [40, 41].

Three-point bending test at elevated temperature

The three-point bending test at elevated temperature is used to determine the behavior and ultimate loading capacity of the PSNS2 and 18TQFR-PSNS2 composites at a relatively high temperature. The results of flexural strength and modulus are shown in

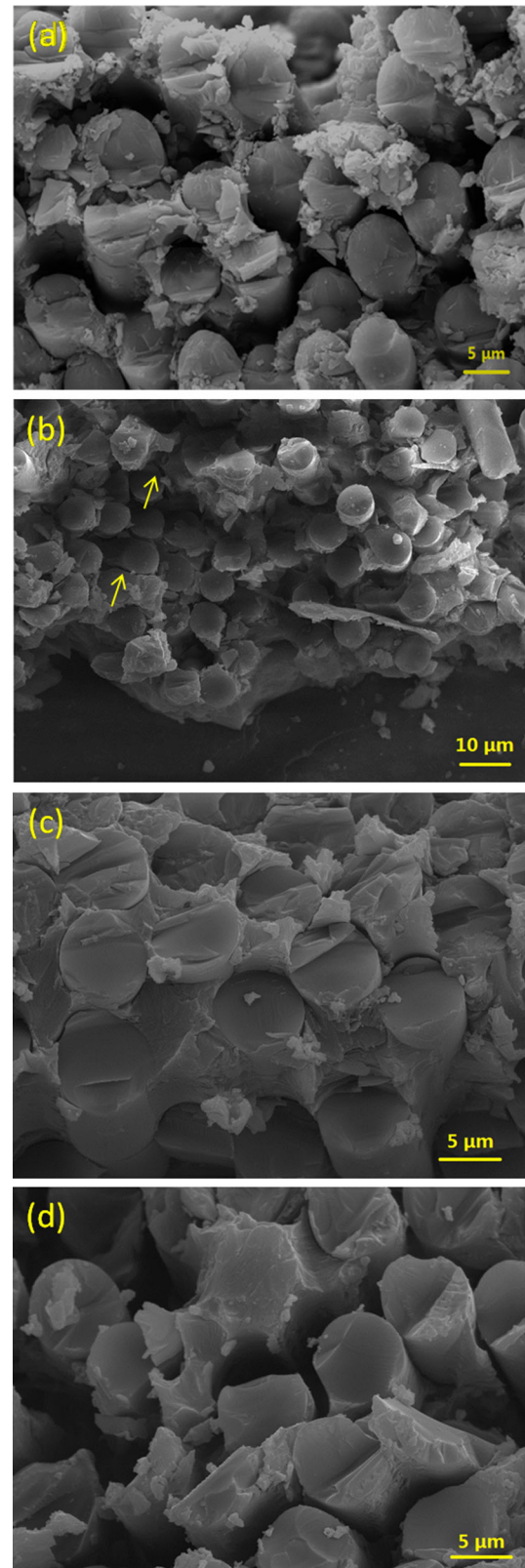


Figure 8 Fracture surface of **a** 18UQFRP, **b** 18TQFRP, **c** 18TQFR-PSNS2 and **d** 18TQFR-PSNS3 by three-point bending test.

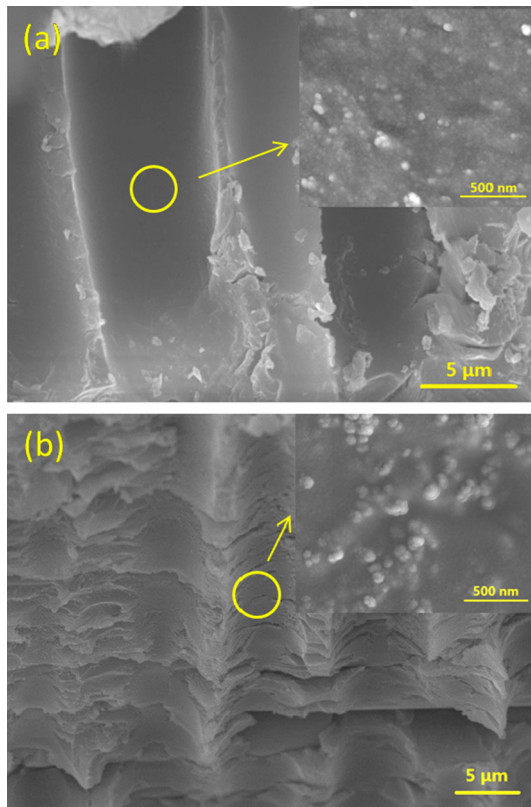


Figure 9 SEM micrographs of **a** 18TQFR-PSNS2 and **b** 18TQFR-PSNS3 on the fiber-matrix interface.

Table 6. It can be seen that flexural strength decreases with increasing testing temperature. The average flexural strength of PSNS2 is decreased from 78 MPa to 41 MPa at 300 °C, about a 47% decrease compared to the strength at room temperature. Furthermore, the average elasticity modulus decreases with increasing temperature and only 44.6% retentated at 300 °C. Figure 10 shows a typical strength-deflection curve of PSNS2 at elevated temperature. As illustrated in Fig. 10, all the specimens show a linear response until the brittle fracture occurring and the flexural extension increases with increasing testing

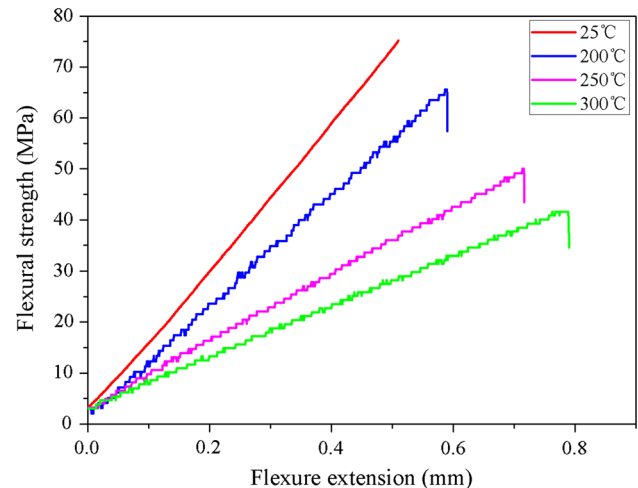


Figure 10 Strength-extension curves of PSNS2 nanocomposites at elevated temperature.

temperature. The fracture surface morphologies for the three-point bending test of PSNS2 samples at elevated temperature are shown in Fig. 11. Figure 11a and b show a corrugated appearance of PSNS2 surface at the room temperature and 200 °C. The ripples are closely spaced in PSNS2 at room temperature as compared to 200 °C, indicating more energy dissipation. The micrographs of PSNS2 at 250 and 300 °C are close agreement with failure behavior of resin at elevated temperature, and it can be seen from the Fig. 11c and d, showing extensive plastic deformation of the matrix. This is due to the resin softening at elevated temperature [8].

The average flexural strength of 18TQFR-PSNS2 decreased from 986 MPa to 499 MPa at 300 °C, about 49% decrease compared to the strength at room temperature. Figure 12 shows a typical strength-deflection curve of the samples. As illustrated in Fig. 12, all the specimens show a linear response until the ductile fracture occur and the flexural extension increased at high temperature. Furthermore, the

Table 6 The flexural strength and modulus of elasticity (E) of PSNS2 and 18TQFR-PSNS2 at elevated temperature

Samples	Temperature (°C)	Flexural strength (MPa)	Elasticity modulus (GPa)
PSNS2	25	78.64 ± 8.06	8.25 ± 0.31
	200	65.05 ± 6.29	5.91 ± 0.28
	250	50.48 ± 4.81	4.33 ± 0.22
	300	41.34 ± 4.19	3.68 ± 0.19
18TQFR-PSNS2	25	986.63 ± 59.60	26.85 ± 0.38
	200	662.13 ± 36.44	24.37 ± 0.58
	250	588.91 ± 36.64	23.26 ± 0.77
	300	499.38 ± 28.07	22.27 ± 1.21

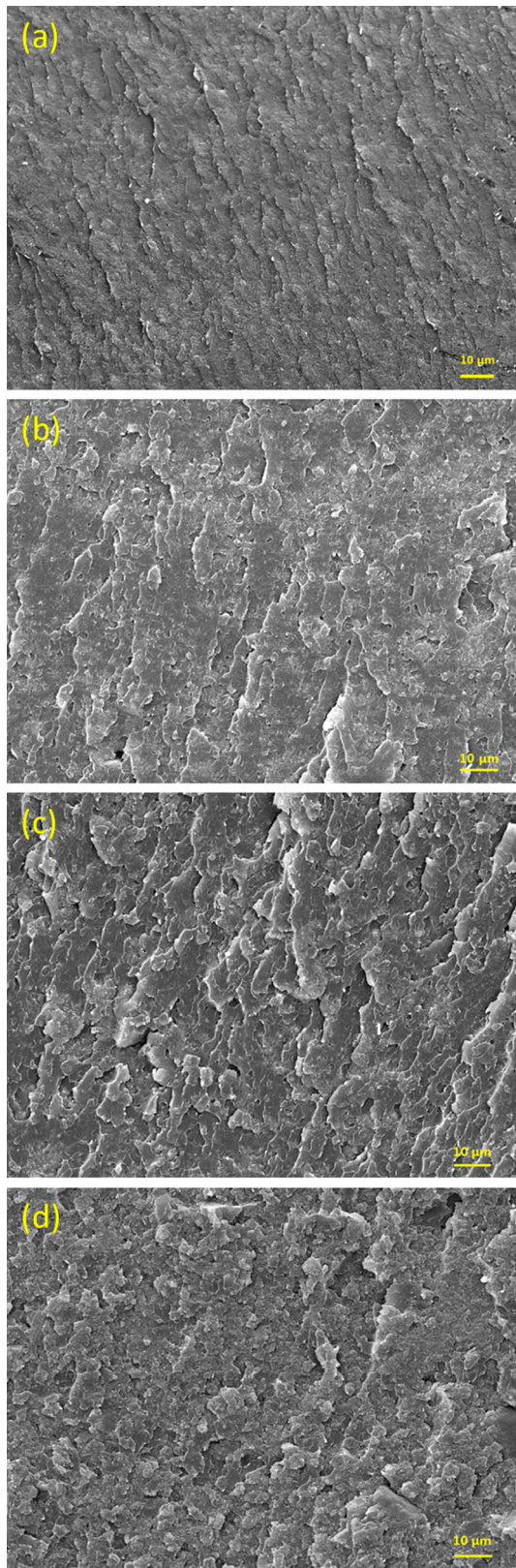


Figure 11 Fracture surface of PSNS2 nanocomposites at **a** room temperature, **b** 200 °C, **c** 250 °C and **d** 300 °C.

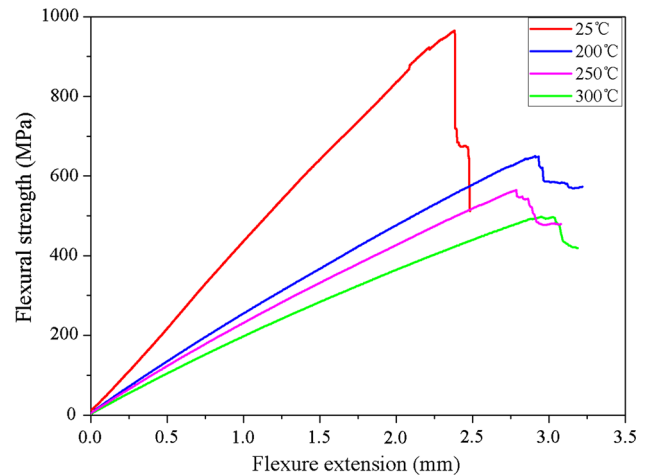


Figure 12 Strength-extension curves of 18TQFR-PSNS2 composites at elevated temperature.

average elasticity modulus decreases with increasing testing temperature, which results from resin softening at elevated temperature [8]. The fracture surface morphologies for the three-point bending test of 18TQFR-PSNS2 samples at elevated temperature are shown in Fig. 13. Figure 13a represents the fracture surfaces of the sample tested at room temperature. The irregular appearance reveals the presence of pulling out fibers, and the fibers are debonded with limited matrix coating. The separation of the fiber yarns due to splitting cracks reveals that cracking in these yarns occur just prior to fracture [7]. The presence of pulling out fiber is revealed by the brushy appearance of the fracture surface and is confirmed by the bare fibers in Fig. 13b, which is a characteristic of brittle fracture. Furthermore, there is little indication of large-scale debonding and evidence of localized matrix fall-out in the fracture region, as soft matrix at high temperature hardly serve to blunt the cracks and make them deflect effectively. There is less splitting in the bundles and more matrix fragment on the bundles compared to the specimens at 200 °C, as seen in Fig. 13c. The matrix looks peeled or torn off indicating a more ductile behavior at 300 °C. Similar fracture events occur and ultimately lead to failure. As shown in Fig. 13d, very smooth fiber imprints were observed on the front where fibers pull out at room temperature. The elevated temperature specimens contain fiber imprints accompanied with matrix deformation on the delaminated surface as seen from Fig. 13e and f. Also in-plane matrix cracks are observed, which may contribute to the loss of mechanical properties at elevated temperature.

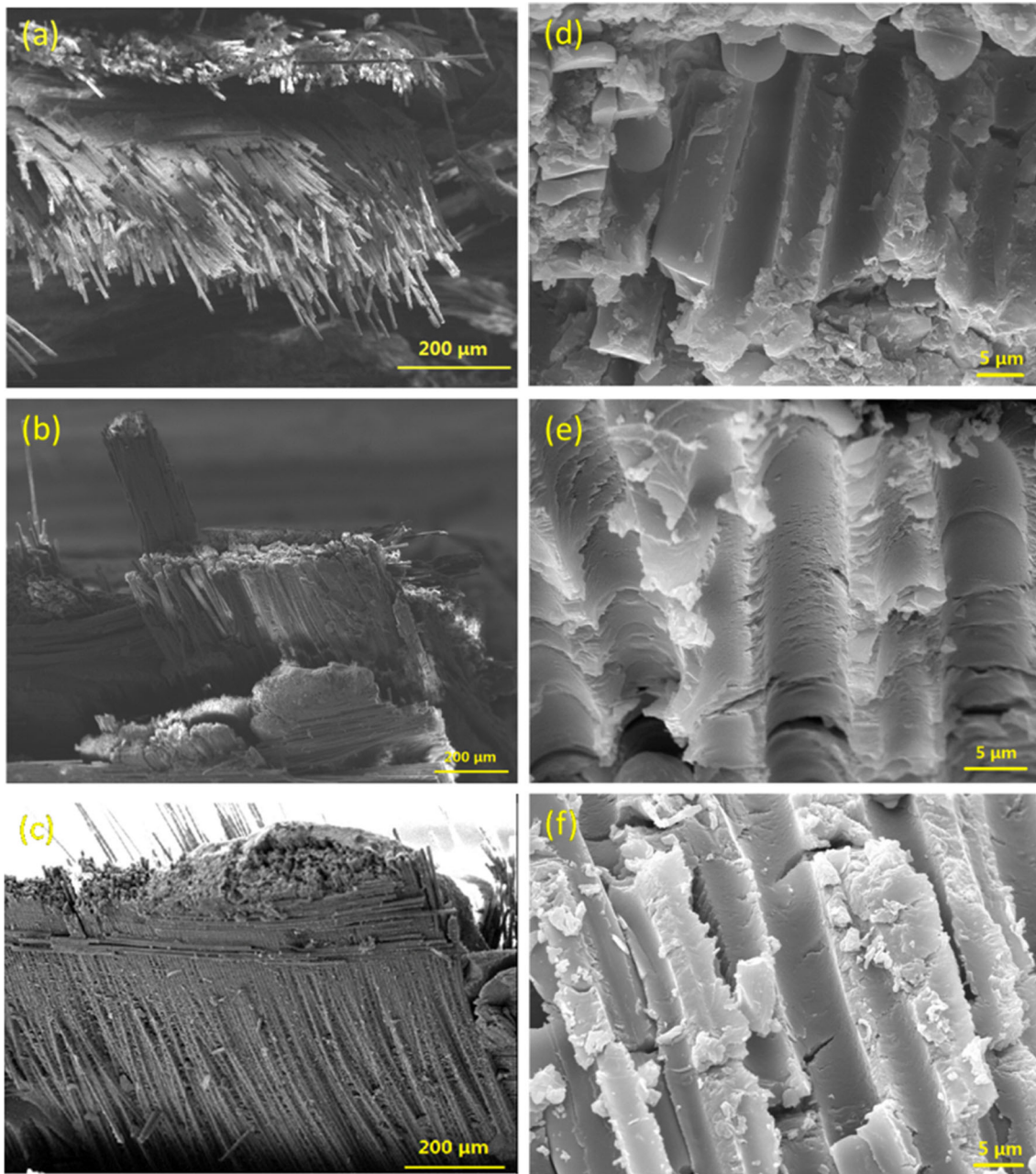


Figure 13 Fracture surface of 18TQFR-PSNS2 composites at **a, d**: room temperature; **b, e** 200 °C; **c, f** 300 °C.

Conclusion

The PI composites reinforced with quartz fabrics and silanized nanosilica with enhanced mechanical properties were achieved at room and elevated temperature. The silanization serves a bridging unit for the nanoparticles, which facilitates a uniform dispersion of SNS in PI matrix. The optimum volume fraction of quartz fabric is 50% and the optimum content of SNS is 2 wt%. The mechanical properties of

quartz fabric reinforced PI composites are noticeably improved after post-curing compared to the untreated counterparts. The flexural strength, elasticity modulus and impact strength of 18TQFR-PSNS2 improve 16.3, 4.2 and 15.8%, respectively, compared to the 18TQFRP composite. Furthermore, the flexural strength of 18TQFR-PSNS2 remains almost 500 MPa at 300 °C. The PI composites reinforced with quartz fabrics and silanized nanosilica has a great application prospect as one of engineering

materials with high strength and high temperature resistance.

Acknowledgements

This work was supported by the Chinese National Natural Science Foundation of China (Grant No. 51402239), and the fund of State Key Laboratory of Solidification Processing in Northwestern Poly-technical University (No. KP201604).

References

- [1] Dinesh KR, Rajesh KP, Devalingam SK, Bankim CR (2016) Mechanical performance of CNT-filled glass fiber/epoxy composite in in situ elevated temperature environments emphasizing the role of CNT content. *Compos Part A* 84:364–376
- [2] Tang YH, Ye L, Zhang Z, Klaus F (2013) Interlaminar fracture toughness and CAI strength of fibre-reinforced composites with nanoparticles—a review. *Compos Sci Technol* 86:26–37
- [3] Sebastian S, Lothar K, Frank S (2014) Nanoparticle reinforced epoxy gelcoats for fiber-plastic composites under multiple load. *Prog Org Coat* 77:1129–1136
- [4] Qing YC, Wang J, Wang HY, Luo F, Zhou WC (2016) Graphene nanosheets/E-glass/epoxy composites with enhanced mechanical and electromagnetic performance. *RCS Adv* 6:80424–80430
- [5] Sanjay M, Arpitha GR, Yogesha B (2015) Study on mechanical properties of natural-glass fibre reinforced polymer hybrid composites: a review. *Mater Today* 2:2959–2967
- [6] João RC, Marco MG, José MP, Fernando AB (2013) Mechanical behaviour of pultruded glass fibre reinforced polymer composites at elevated temperature: experiments and model assessment. *Compos Struct* 98:303–313
- [7] Allan M, Swetha S, Gerard VE, Brahim B (2016) Flexural behavior of an FRP sandwich system with glass-fiber skins and a phenolic core at elevated in-service temperature. *Compos Struct* 152:96–105
- [8] John M, Zouheir F, Cheung P, Kamran B (2014) A microscopic investigation of failure mechanisms in a triaxially braided polyimide composite at room and elevated temperatures. *Mater Design* 53:1026–1036
- [9] Sethi S, Rathore DK, Ray BC (2015) Effects of temperature and loading speed on interface-dominated strength in fibre/polymer composites: an evaluation for in situ environment. *Mater Des* 65:617–626
- [10] Yao YM, Zeng XL, Guo K, Sun R, Xu JB (2015) The effect of interfacial state on the thermal conductivity of functionalized Al₂O₃ filled glass fibers reinforced polymer composites. *Compos Part A* 69:49–55
- [11] Lv M, Wang QH, Wang TM, Liang YM (2015) Effects of atomic oxygen exposure on the tribological performance of ZrO₂-reinforced polyimide nanocomposites for low earth orbit space applications. *Compos Part B* 77:215–222
- [12] Mallakpour S, Dinari M (2012) Fabrication of polyimide/titania nanocomposites containing benzimidazole sidegroups via sol-gel process. *Prog Org Coat* 75:373–378
- [13] Chen C, Justice R, Schaefer DW, Baur JW (2008) Highly dispersed nanosilica-epoxy resins with enhanced mechanical properties. *Polymer* 49:3805–3815
- [14] Ma J, Qi XW, Zhao YL, Dong Y, Song LZ, Zhang QL, Yang YL (2016) Polyimide/mesoporous silica nanocomposites: characterization of mechanical and thermal properties and tribochemistry in dry sliding condition. *Mater Design* 108:538–550
- [15] Wang RL, Bao S, Liu FW, Jiang XZ, Zhang QH, Sun B, Zhu MF (2013) Wear behavior of light-cured resin composites with bimodal silica nanostructures as fillers. *Mater Sci Eng C* 33:4759–4766
- [16] Sprenger S (2013) Epoxy resins modified with elastomers and surface-modified silica nanoparticles. *Polymer* 54:4790–4797
- [17] Sprenger S (2014) Fiber-reinforced composites based on epoxy resins modified with elastomers and surface-modified silica nanoparticles. *J Mater Sci* 49:2391–2402. doi:[10.1515/opli-2016-0018](https://doi.org/10.1515/opli-2016-0018)
- [18] Sprenger S, Martin HK, Volker A (2014) Carbon fiber-reinforced composites using an epoxy resin matrix modified with reactive liquid rubber and silica nanoparticles. *Compos Sci Technol* 105:86–95
- [19] Yang Y, Lu CX, Su XL, Wu GP, Wang XK (2007) Effect of nano-SiO₂ modified emulsion sizing on the interfacial adhesion of carbon fibers reinforced composites. *Mater Lett* 61:3601–3604
- [20] Liaw DJ, Wang KL, Huang YC, Lee KR, Lai JY, Ha CS (2012) Advanced polyimide materials: syntheses, physical properties and applications. *Prog Polym Sci* 37:907–974
- [21] Ding MX (2007) Isomeric polyimides. *Prog Polym Sci* 32:623–668
- [22] Chung EY, Choi SM, Sim HB, Kim KK, Kim DS, Kim KJ, Yi MH (2005) Synthesis and characterization of novel photosensitive polyimide based on 5-(2,5-dioxotetrahydrofuryl)-3-methyl-3-cyclohexene-1,2-dicarboxylic anhydride. *Polym Adv Technol* 16:19–23
- [23] Wang WC, Ong GT, Lim SL, Vora RH, Kang ET, Neo KG (2003) Synthesis and characterization of fluorinated

- polyimide with grafted poly(N-isopropylacrylamide) side chains and the temperature-sensitive microfiltration membranes. *Ind Eng Chem Res* 42:3740–3749
- [24] Hsiao SH, Liou GS, Chang LM (2001) Synthesis and properties of organosoluble polyimide/clay hybrid. *J Appl Polym Sci* 80:2067–2072
- [25] Zhang XR, Pei XQ, Wang QH (2009) Friction and wear studies of polyimide composites filled with short carbon fibers and graphite and micro SiO₂. *Mater Design* 30:4414–4420
- [26] Song FZ, Wang QH, Wang TM (2016) High mechanical and tribological performance of polyimide nanocomposites reinforced by chopped carbon fibers in adverse operating conditions. *Compos Sci Technol* 134:251–257
- [27] Shiina Y, Morikawa A (2011) Preparation and properties of polyimide-silica hybrid films with conjugation of the polyimide and silica by a sol-gel process using 3-(triethoxysilyl)propyl succinic anhydride. *React Funct Polym* 71:85–94
- [28] Li Y, Fu SY, Li YQ, Pan QY, Xu G, Yue CY (2007) Improvements in transmittance, mechanical properties and thermal stability of silica-polyimide composite films by a novel sol-gel route. *Compos Sci Technol* 67:2408–2416
- [29] Liu LP, Lv FZ, Li PG, Ding L, Tong WS, Chu PK, Zhang YH (2016) Preparation of ultra-low dielectric constant silica/polyimide nanofiber membranes by electrospinning. *Compos Part A* 84:292–298
- [30] Huang JY, Li XH, Luo LB, Wang HN, Wang X, Li K, Zhang CL, Liu XY (2014) Releasing silica-confined macromolecular crystallization to enhance mechanical properties of polyimide/silica hybrid fibers. *Compos Sci Technol* 101:24–31
- [31] Wang J, Zhou WC, Luo F, Zhu DM, Qing YC (2017) Dielectric and microwave absorbing properties of quartz fiber/amorphous carbon/polyimide composites at elevated temperature. *J Nanosci Nanotechnol* 17:3751–3758
- [32] Gao SL, Mader E, Plonka R (2008) Nanocomposite coatings for healing surface defects of glass fibers and improving interfacial adhesion. *Compos Sci Technol* 68:2892–2901
- [33] Zhang H, Zhang Z, Friedrich K, Eger C (2006) Property improvements of in situ epoxy nanocomposites with reduced interparticle distance at high nanosilica content. *Acta Mater* 54:1833–1842
- [34] Chira A, Kumar A, Vlach T, Laiblová L, Škapin AS, Hájek P (2016) Property improvements of alkali resistant glass fibers/epoxy composite with nanosilica for textile reinforced concrete applications. *Mater Design* 89:146–155
- [35] Huxtable ST, Cahill DG, Shenogin S, Xue L, Ozisik R, Barone P, Usrey M, Strano MS, Siddons G, Shim M (2003) Interfacial heat flow in carbon nanotube suspensions. *Nat Mater* 2:731–734
- [36] Miyagawa H, Drzal LT (2004) Thermo-physical and impact properties of epoxy nanocomposites reinforced by single-wall carbon nanotubes. *Polymer* 45:5163–5170
- [37] Gao H, Yorifuji D, Jiang ZH, Ando SJ (2014) Thermal and optical properties of hyperbranched fluorinated polyimide/mesoporous SiO₂ nanocomposites exhibiting high transparency and reduced thermo-optical coefficients. *Polymer* 55:2848–2855
- [38] Faber KT, Evans AG (1983) Crack deflection processes II. Experiment. *Acta Metall* 31:577–584
- [39] Chris JC, Eva M (2002) Hybrid inorganic-organic materials based on a 6FDA-6FpDA-DABA polyimide and silica: physical characterization studies. *Polymer* 43:2385–2400
- [40] Hakamy A, Shaikh FUA, Low IM (2015) Thermal and mechanical properties of NaOH treated hemp fabric and calcined nanoclay-reinforced cement nanocomposites. *Mater Design* 80:70–81
- [41] Hakamy A, Shaikh FUA, Low IM (2014) Thermal and mechanical properties of hemp fabric-reinforced nanoclay-cement nanocomposites. *J Mater Sci* 49:1684–1694. doi:[10.1007/s10853-013-7853-0](https://doi.org/10.1007/s10853-013-7853-0)